

Charged-current reactions in the supernova neutrino-sphere

Ermal Rrapaj,^{1,2,*} J. W. Holt,¹ Alexander Bartl,^{3,4} Sanjay Reddy,^{2,1,†} and A. Schwenk^{3,4}

¹*Department of Physics, University of Washington, Seattle, WA*

²*Institute for Nuclear Theory, University of Washington, Seattle, WA*

³*Institut für Kernphysik, Technische Universität Darmstadt, 64289 Darmstadt, Germany*

⁴*ExtreMe Matter Institute EMMI, GSI Helmholtzzentrum für
Schwerionenforschung GmbH, 64291 Darmstadt, Germany*

Abstract

We calculate neutrino absorption rates due to charged-current reactions $\nu_e + n \rightarrow e^- + p$ and $\bar{\nu}_e + p \rightarrow e^+ + n$ in the outer regions of a newly born neutron star called the neutrino-sphere. To improve on recent work which has shown that nuclear mean fields enhance the ν_e cross-section and suppress the $\bar{\nu}_e$ cross-section, we employ realistic nucleon-nucleon interactions that fit measured scattering phase shifts. Using these interactions we calculate the momentum-, density-, and temperature-dependent nucleon self-energies in the Hartree-Fock approximation. A potential derived from chiral effective field theory and a pseudo-potential constructed to reproduce nucleon-nucleon phase shifts at the mean-field level are used to study the equilibrium proton fraction and charged-current rates. We compare our results to earlier calculations obtained using phenomenological mean-field models and to those obtained in the virial expansion valid at low density and high temperature. In the virial regime our results are consistent with previous calculations, and at higher densities relevant for the neutrino sphere, $\rho \gtrsim 10^{12}$ g/cm³, we find the difference between the ν_e and $\bar{\nu}_e$ absorption rates to be larger than predicted earlier. Our results may have implications for heavy-element nucleosynthesis in supernovae, and for supernova neutrino detection.

arXiv:1408.3368v3 [nucl-th] 1 Apr 2015

* ermal@uw.edu

† sareddy@u.washington.edu

I. INTRODUCTION

The neutrino opacity of dense matter plays a central role in supernovae, associated nucleosynthesis, and the subsequent evolution of the newly born neutron star called the proto-neutron star (PNS). Neutrino interactions at the high densities and temperatures of relevance are influenced by matter degeneracy, inter-particle correlations due to strong and electromagnetic interactions, and by multi-particle excitations [1–11]. Supernova and PNS simulations that include these corrections have found them to play a role in shaping the temporal and spectral aspects of neutrino emission [4, 12–14]. Of particular interest to our study here are the spectra of electron and anti-electron neutrinos, ν_e and $\bar{\nu}_e$, which decouple in the outer region of the PNS called the neutrino-sphere. Here, the reactions $\nu_e + n \rightarrow e^- + p$ and $\bar{\nu}_e + p \rightarrow e^+ + n$ are an important source of neutrino opacity, and their rates directly influence the mean energy of ν_e and $\bar{\nu}_e$ neutrinos [1–4]. The mean neutrino energy can in turn impact supernova dynamics [15], supernova nucleosynthesis [16, 17], and influence the number of neutrinos detectable from a supernova in terrestrial neutrino detectors [18].

Since matter is neutron-rich in the neutrino-sphere, the reaction $\nu_e + n \rightarrow e^- + p$ is favored over $\bar{\nu}_e + p \rightarrow e^+ + n$, and on general grounds we can expect that $\langle\sigma_{\nu_e}\rangle > \langle\sigma_{\bar{\nu}_e}\rangle$, where $\langle\sigma_{\nu_e}\rangle$ and $\langle\sigma_{\bar{\nu}_e}\rangle$ are the thermally averaged neutrino and anti-neutrino cross-sections, respectively. The corresponding root-mean-square (rms) energies of neutrinos emerging from the neutrino-sphere will satisfy the following inequality $\epsilon_{\bar{\nu}_e} > \epsilon_{\nu_e}$. It is now well established, through parametric studies and simulations, that nucleosynthesis in the neutrino-driven wind (NDW) is very sensitive to the difference $\delta\epsilon = \epsilon_{\bar{\nu}_e} - \epsilon_{\nu_e}$. Neutron-rich conditions in the material ejected by the neutrino-driven wind, a prerequisite for the r-process, is only achieved when $\delta\epsilon > 4(m_n - m_p) \simeq 5$ MeV [16, 17]. Parametric studies indicate a robust r-process in the NDW is only realized for an electron fraction $Y_e \lesssim 0.4$ which requires even larger $\delta\epsilon$ [19, 20]. However, recent simulations of supernova and PNS evolution do not achieve these conditions, instead they predict $Y_e > 0.45$ [13, 17, 21]. This difficulty has led to a renewed interest in charged-current reactions in the neutrino-sphere to better determine the differences in neutrino spectra.

The role of nuclear interactions in determining the charged-current rates in dense neutron-rich matter was first studied in [1]. Subsequently, it was recognized [22, 23] that the difference in the neutron and proton interaction energies enhances the electron neutrino absorption cross-section and simultaneously suppresses the cross-section for the absorption of anti-electron neutrinos. Simple phenomenological models based on the relativistic mean field (RMF) theory [23], and a model independent approach

based on the virial expansion valid at low density and high temperatures [24] were used to calculate the difference between the neutron and proton interaction energies. Using these inputs it was found that the electron neutrino absorption rate in the neutrino-sphere for typical thermal neutrinos with energy $\simeq 10$ MeV could be enhanced by a factor of $2 - 4$, while the absorption rates for anti-electron neutrinos were found to be suppressed by as much as an order of magnitude [22–24]. Due to this suppression, other processes including the neutral-current processes such as $\bar{\nu}_e + \nu_e + N + N \rightarrow N + N$ were found to play a role in determining the $\bar{\nu}_e$ spectra, which were consequently found to be very similar to the spectra expected for ν_μ and ν_τ .

In this article, we improve on these earlier studies by using realistic nuclear interactions that can reproduce nucleon-nucleon (NN) phase shifts to compute the nucleon self-energies and the equation of state of hot and dense matter expected in the neutrino-sphere. We use the potential developed by Entem and Machleidt [25] within the framework of chiral effective field theory (EFT) at next-to-next-to-next-to-leading order (N³LO) in the chiral expansion. This low-momentum potential is able to reproduce low-energy phase shifts without a strong repulsive core and it is expected that many-body perturbation theory provides a reasonable description of matter at moderate density and temperature [26–37]. To assess the convergence of many-body perturbation theory in the particle-particle channel (the ladder summation) for the partially degenerate conditions encountered in the neutrino-sphere, we define and use a pseudo-potential, which is given directly in terms of NN phase shifts obtained from the partial-wave analysis (PWA) of the Nijmegen group [38]. The composition of matter, and the medium-induced self-energies are obtained using finite-temperature perturbation theory in the Hartree-Fock (HF) approximation. This allows us to calculate the in-medium Green’s functions for neutrons and protons, and the density-, temperature-, and momentum-dependent nucleon dispersion relations are naturally incorporated in calculations of the charged-current cross-sections for ν_e and $\bar{\nu}_e$. We also present new results, using the formalism developed in Ref. [11], for the neutrino pair absorption mean free path for the reaction $\bar{\nu}_e + \nu_e + N + N \rightarrow N + N$, which improves upon earlier work by properly accounting for nucleon-nucleon interactions and nucleon self-energies in the medium.

In Sec. II we describe the kinematics of charged-current reactions and highlight the importance of nucleon dispersion relations. The nucleon dispersion relation and the composition of matter in the neutrino-sphere are calculated in Sec. III, where we also briefly discuss the NN interactions used and assess the validity of the HF approximation for the relevant conditions. In Sec. IV the neutrino-absorption

rates using the HF self-energies are calculated and compared to results obtained in earlier work. In Sec. V we discuss the implications of our findings and identify areas where improvements are necessary. Finally, we note that throughout we use natural units: we set $\hbar = 1$, the speed of light $c = 1$ and the Boltzmann constant $k_B = 1$. Energy and temperature are measured in MeV, and the density is measured in units of nucleons per fm^3 .

II. KINEMATICS

We begin with a general discussion of the kinematics of charged-current reactions to highlight the importance of nuclear interactions. Kinematic restrictions for the charged-current reactions $\nu_e + n \rightarrow e^- + p$ and $\bar{\nu}_e + p \rightarrow e^+ + n$ are relevant, because the neutrino energy is comparable to the typical energy and momentum scales in the hot and dense plasma in the neutrino-sphere. Due to strong electron degeneracy, final-state blocking suppresses the ν_e absorption when the neutrino energy is comparable or smaller than the electron Fermi energy. Similarly, $\bar{\nu}_e$ absorption requires a neutrino energy large enough to overcome the energy difference between the proton in the initial state and the neutron plus positron energy in the final state. These constraints are depicted in Fig. 1, where we illustrate energy and momentum conservation for an incoming neutrino of energy $E_\nu = 24$ MeV; this is the typical thermal energy of the neutrino for an ambient temperature of $T = 8$ MeV. The x -axis is the magnitude of the momentum transferred to the nucleons, $\vec{q} = \vec{k}_\nu - \vec{k}_e$, where \vec{k}_ν and \vec{k}_e are the ν_e ($\bar{\nu}_e$) and final state e^- (e^+) lepton momenta, respectively. The y -axis is the final-state lepton energy E_e . The shaded area enclosed by the solid black lines is the region allowed by lepton kinematics for an incoming neutrino with $E_\nu = 24$ MeV.

The reaction can proceed when the allowed regions for nucleon and lepton kinematics overlap. Energy and momentum constraints imposed by the nucleons for the $\nu_e + n \rightarrow e^- + p$ and $\bar{\nu}_e + p \rightarrow e^+ + n$ reactions are shown by the regions enclosed by the dashed blue and red curves, respectively. For the ν_e reaction, the blue region is defined by the equation $E_n(|\vec{k}|) - E_p(|\vec{k} + \vec{q}|) = -\omega$, and for the $\bar{\nu}_e$ reaction the red region is defined by $E_p(|\vec{k}|) - E_n(|\vec{k} + \vec{q}|) = -\omega$, where $\omega = E_\nu - E_e$ is the energy transferred to the nucleons. When nuclear interactions are neglected, the neutron and proton single-particle energies are given by $E_n(|\vec{k}|) = M_n + k^2/2M_n$ and $E_p(|\vec{k}|) = M_p + k^2/2M_p$, respectively. In this case, the allowed kinematic region for the ν_e and $\bar{\nu}_e$ are similar and the small difference arises solely due to the small neutron-proton mass difference.

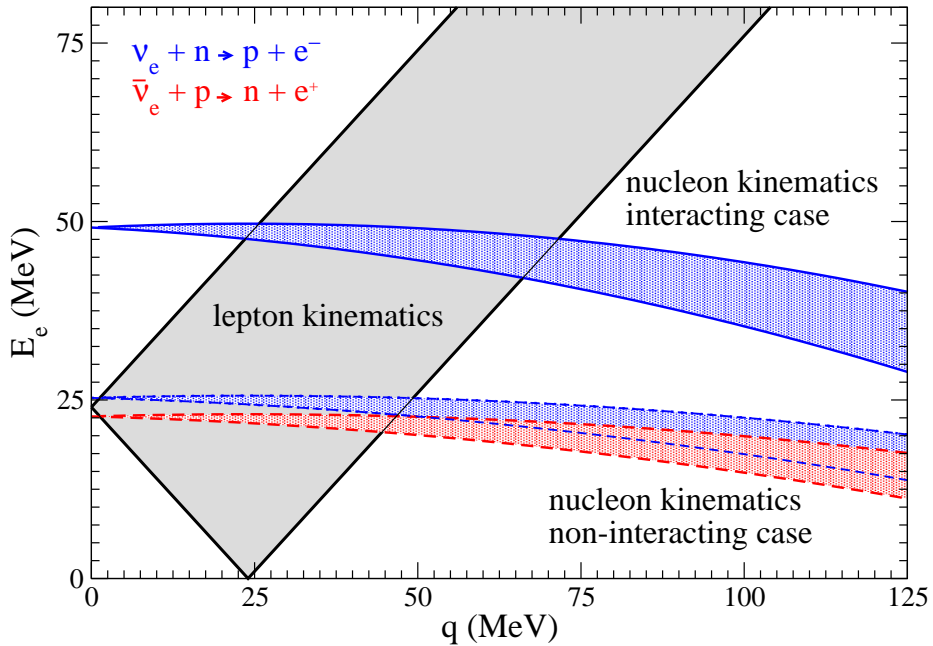


FIG. 1. (Color online) Energy and momentum constraints on the charged-current reactions for conditions discussed in the text. Reactions are possible when the allowed region for lepton kinematics, shown by the shaded region enclosed by the black lines, overlaps the allowed region for nucleon kinematics, shown by the regions enclosed by blue and red lines corresponding to the ν_e and $\bar{\nu}_e$ reactions, respectively. The region enclosed by the solid blue lines includes the nuclear self-energy difference for the transition $n \rightarrow p$ associated with the ν_e reaction, and regions enclosed by the dashed lines are for non-interacting nucleons. The $p \rightarrow n$ transition associated with the $\bar{\nu}_e$ reaction is kinematically forbidden as there is no overlap when nucleon self-energy corrections are included.

In an interacting system, the single-particle energy is given by

$$E_{i=n,p}(|\vec{k}|) = M_i + \frac{k^2}{2M_i} + \Sigma_i(k) \equiv \varepsilon_i(k) + M_i, \quad (1)$$

where $\Sigma_i(k)$ is the momentum-, density-, and temperature-dependent self-energy (we note that in general, the self-energy will also be energy-dependent, but in the Hartree-Fock approximation employed in the present study this does not arise). At the densities $\rho \simeq 10^{11} - 10^{13} \text{ g/cm}^3$ and temperatures $T \simeq 3 - 10 \text{ MeV}$ of interest in the neutrino-sphere, matter is very neutron-rich with an electron fraction Y_e of only a few percent (note that charge neutrality requires the proton fraction $Y_p = Y_e$). Due to

this large asymmetry, the proton and neutron self-energies are not equal, $\Sigma_n(k) \neq \Sigma_p(k)$. Both neutron and proton energies are shifted downwards by the nuclear interaction at the densities and temperatures encountered in the neutrino-sphere, i.e., $\Sigma_i < 0$, because NN interactions are on average attractive at the relevant low momenta ($k < 200$ MeV). However, the energy shift is much larger for the protons and $\Sigma_n - \Sigma_p > 0$ because of the denser neutron background and the additional attraction in the neutron-proton interaction. This energy difference is related to the potential part of the nuclear symmetry energy — in neutron-rich matter it costs nuclear interaction energy to convert protons to neutrons, and there is an energy gain resulting from the conversion of neutrons to protons. The resulting change in the reaction Q value modifies the relative ν_e and $\bar{\nu}_e$ absorption rates as described below.

Using calculations of $\Sigma_n(k)$ and $\Sigma_p(k)$, which will be discussed in detail in Sec. III, we illustrate the change in reaction kinematics in Fig. 1 by enclosing the allowed nucleon kinematic regions (using the same color legend) by solid lines. The Q value for the reaction at $q = 0$ is the energy shift $\Sigma_n(k) - \Sigma_p(k) \simeq 30$ MeV which is much larger than the rest mass difference $M_n - M_p = 1.3$ MeV. This large energy gain associated with $n \rightarrow p$ conversion shifts the outgoing electron energy to larger values and the overlap region between lepton and nucleon kinematic regions is enhanced. Further, the higher Q value also helps overcome the Pauli blocking in the final state for the degenerate electrons with $\mu_e/T \gtrsim 3 - 10$. In contrast, the $\bar{\nu}_e$ reaction is now kinematically forbidden because the $\bar{\nu}_e$ energy $E_{\nu} = 24$ MeV is insufficient to overcome the energy threshold $\simeq 30$ MeV to convert protons to neutrons.

III. NUCLEON SINGLE-PARTICLE ENERGIES IN THE NEUTRINO-SPHERE

Nucleon dispersion relations are modified in a hot and dense medium due to nuclear interactions. In this section, we calculate these modifications using realistic nuclear interactions in the HF approximation. The self-consistent HF self-energy Σ_{HF} is defined through the Feynman diagrams shown in Fig. 2. We calculate Σ_{HF} using the finite-temperature imaginary-time formalism and find the standard expression

$$\Sigma(\vec{k}) = \not{\int} \frac{d^4 k'}{(2\pi)^4} \bar{V}\left(\frac{\vec{k}-\vec{k}'}{2}, \frac{\vec{k}-\vec{k}'}{2}\right) = \int \frac{d^3 k'}{(2\pi)^3} \bar{V}\left(\frac{\vec{k}-\vec{k}'}{2}, \frac{\vec{k}-\vec{k}'}{2}\right) f(\xi(\vec{k}')), \quad (2)$$

where $\xi(\vec{k}') = \varepsilon(\vec{k}') - \mu = k'^2/2M + \Sigma(k') - \mu$ is the single-particle energy measured with respect to the non-relativistic chemical potential (the rest mass of the nucleon has been subtracted). The sum over Matsubara frequencies is performed to obtain the Fermi distribution function $f(\xi(k'))$. Since the

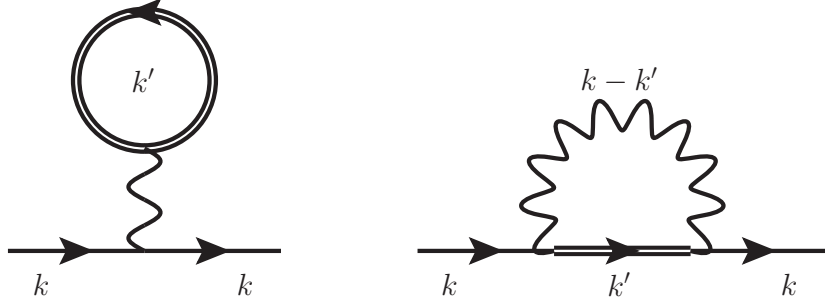


FIG. 2. Feynman diagrams depicting the self-consistent HF self-energy. The double lines are the dressed nucleon propagators and wavy lines represent the NN interaction.

potential \bar{V} is antisymmetrized, both contributions in Fig. 2 (the Hartree contribution on the left and the Fock contribution on the right) are contained in the single expression above. We use a spherical decomposition to represent the anti-symmetrized potential in a partial-wave basis:

$$\langle \vec{p} S m_s T | \bar{V} | \vec{p}' S m'_s T \rangle = (4\pi)^2 \sum_{l,m,l',m',J,M} i^{l'-l} Y_l^m(\hat{p}) Y_{l'}^{m'*}(\hat{p}') C_{lmSm_s}^{JM} C_{l'm'Sm'_s}^{JM} \langle p | V_{ll'S}^{JT} | p' \rangle (1 - (-1)^{l+S+T}), \quad (3)$$

where \vec{p} and \vec{p}' are relative momenta and $\bar{V} \equiv V(1 - P_{12}) = V(1 - (-1)^{l+S+T})$, with P_{12} the particle-exchange operator. The other symbols appearing in Eq. (3) have the standard meaning: l, S, J and T are the relative orbital angular momentum, spin, total angular momentum and total isospin quantum numbers of the nucleon pair, and the projections of \vec{S} and \vec{l} onto the z -axis are given by the quantum numbers m_s and m , respectively.

For pure neutron matter the self-energy can be written as

$$\Sigma_n(\vec{k}) = \frac{1}{2\pi} \int_0^\infty k'^2 dk' \int_{-1}^1 d \cos \theta_{k'} f(\xi(\vec{k}')) \sum_{l,S,J} (2J+1) \langle |(\vec{k} - \vec{k}')/2| | \bar{V}_{US}^{J1} | |(\vec{k} - \vec{k}')/2| \rangle, \quad (4)$$

where $\theta_{k'}$ is the angle between \vec{k}' and \vec{k} . The self-consistent solution to Eq. (4) can be obtained by iteration. To simplify notation we set $p = |\frac{1}{2}(\vec{k} - \vec{k}')|$ in the following. In asymmetric matter, containing neutrons and protons we obtain the following coupled equations:

$$\Sigma_{m_t}(\vec{k}) = \frac{1}{2\pi} \int_0^\infty k'^2 dk' \int_{-1}^1 d \cos \theta_{k'} \sum_{l,S,J,T,m'_t} (2J+1) |C_{\frac{1}{2}m_t \frac{1}{2}m'_t}^{T m_t + m'_t}|^2 \langle p | \bar{V}_{US}^{JT} | p \rangle f(\varepsilon_{m'_t}(\vec{k}') - \mu_{m'_t}), \quad (5)$$

where m_t and m'_t label the isospin of the external and intermediate-state nucleon, respectively.

At low densities and high temperatures, where the neutron fugacity satisfies $z_n = e^{\mu_n/T} \ll 1$, the virial expansion provides a model-independent benchmark [39, 40]. This allows us to assess the validity of the HF approximation at densities characteristic of the neutrino-sphere. First, we analyze the HF predictions for the energy per particle in pure neutron matter in the density range $n_B = 0.001 - 0.02 \text{ fm}^{-3}$ and temperature range $T = 5 - 10 \text{ MeV}$. To calculate the energy density in the HF approximation we use two approaches. In the first, we employ the chiral N³LO NN potential of Ref. [25], and in the second approach we define and use the pseudo-potential.

In the HF calculation, the N³LO potential is treated in the Born approximation. In contrast, the pseudo-potential defined by the relation

$$\langle p | V_{llSJ}^{pseudo} | p \rangle = -\frac{\delta_{lSJ}(p)}{pM}, \quad (6)$$

is constructed from the measured nucleon-nucleon phase shifts $\delta_{lSJ}(p)$ and should be viewed as including a resummation of the ladder diagrams in the particle-particle channel. It is also known to correctly predict the energy shift in a system containing Fermions interacting strongly with a heavy impurity and is known in the context of condensed matter physics as Fumi's theorem [41]. In the following we show that the pseudo-potential when used in the HF approximation reproduces the energy shift predicted by the virial expansion which is known to be exact in the limit of low density and high temperature.

In the virial expansion, two-body interactions are included through the second virial coefficient b_2 , which is directly related to scattering phase shifts and is given by

$$b_2 = \frac{1}{\pi\sqrt{2}T} \int_0^\infty d\epsilon e^{-\epsilon/2T} \sum_{lSJ} (2J+1) \delta_{lSJ}(\epsilon) - 2^{-5/2}, \quad (7)$$

where $\epsilon = p^2/2m$ is the kinetic energy and the sum is over allowed partial waves. The number density n and the energy density \mathcal{E} are calculated in terms of the b_2 coefficient and are given by [40]

$$\begin{aligned} n &= \frac{2}{\lambda^3} (z_n + 2z_n^2 b_2), \\ \mathcal{E} &= \frac{3T}{\lambda^3} \left[z_n + z_n^2 \left(b_2 - \frac{2}{3} T b'_2 \right) \right], \end{aligned} \quad (8)$$

where $b'_2 = db_2/dT$. The respective expressions for the HF calculation in pure neutron matter are

$$\begin{aligned} n &= 2 \int \frac{dk^3}{(2\pi)^3} f(\xi(\vec{k})), \\ \mathcal{E} &= 2 \int \frac{dk^3}{(2\pi)^3} \left(\varepsilon(\vec{k}) - \frac{1}{2} \Sigma_n(\vec{k}) \right) f(\xi(\vec{k})). \end{aligned} \tag{9}$$

A detailed study of low-density hot matter in the virial expansion is presented in Refs. [39, 40]. Here we consider neutron matter and use the second virial coefficient computed in Ref. [40] to compare with the results obtained using the chiral NN potential and the pseudo-potential in the HF approximation. Results for $T = 8 \text{ MeV}$ are displayed in Fig. 3, which shows the change in the energy per particle due to NN interactions. At very low densities (with corresponding fugacities $z < 0.25$), the virial equation of state is well reproduced at the HF level when the pseudo-potential is used, in agreement with previous statistical-mechanics consistency checks [42, 43]. At the breakdown scale of the virial expansion $e^{\mu/T} \sim 0.5$, the pseudo-potential predicts additional attraction over the virial equation of state due to using full Fermi-Dirac distribution functions. On the other hand, the chiral NN potential when used in the HF approximation significantly underestimates the strength of the attractive mean field at low densities and therefore provides a conservative upper bound on the energy per particle at temperatures and densities beyond the scope of the virial expansion. Higher-order perturbative contributions from chiral NN interactions are attractive and could lead to a narrower uncertainty band for the energy per particle. We omit contributions from three-neutron forces, which are small at these low densities.

A comparison between the second-order virial calculation and the HF calculation of matter with a finite proton fraction $Y_p = n_p/(n_p + n_n)$, where n_n and n_p are the neutron and proton densities, is complicated by the presence of the deuteron bound state. The HF description solely in terms of neutrons and protons will fail at low temperature and density when there is a large abundance of deuterons and light nuclei. However, on general grounds we expect the abundance of weakly bound states such as the deuteron to decrease rapidly with increasing temperature and density. The second-order virial calculation provides a correct description of deuterons at low density and moderate temperature, but it does not capture the physics relevant to the dissolution of weakly bound states with increasing density. Finite-density effects due to Pauli blocking of intermediate states in the T -matrix and modifications to the nucleon propagators alter the scattering in the medium at low momentum. Recent calculations

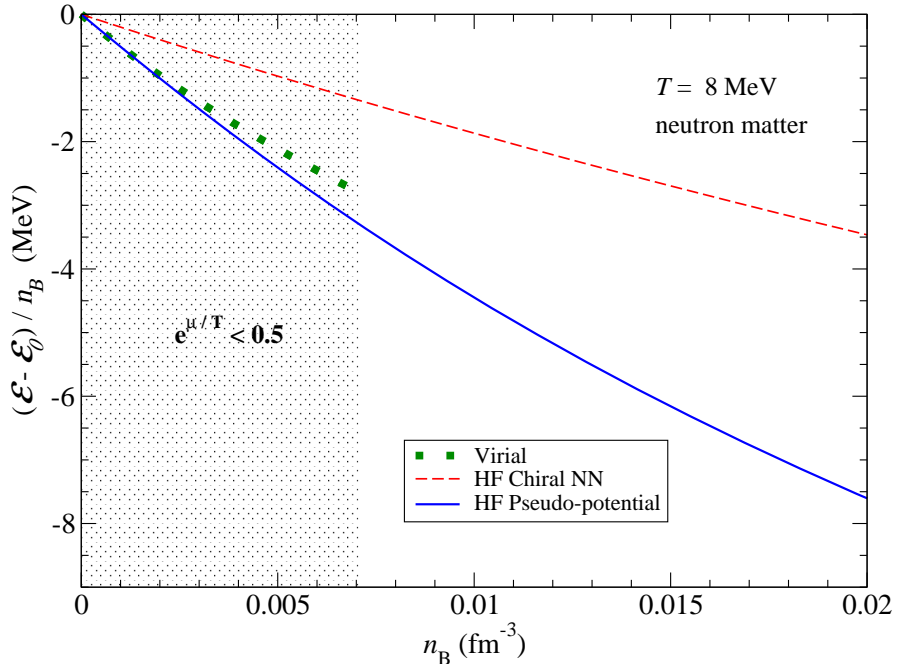


FIG. 3. (Color online) Change in the energy per particle of neutron matter from NN interactions in the Hartree-Fock (HF) approximation. Results for both the chiral NN potential and the pseudo-potential are shown and compared to the model-independent virial equation of state [40]. The shaded area denotes the density region in which the fugacity $z < 0.5$.

have shown that this leads to a decrease in the binding energy of light nuclei [44]. These results indicate that the deuteron abundance is suppressed for $n_B \gtrsim 0.005 \text{ fm}^{-3}$ [44–46] even at relatively low temperatures. Since the typical densities encountered in the neutrino-sphere are larger, especially during the proto-neutron star phase, in the following we will neglect the deuteron pole and calculate the nucleon self-energies in the HF approximation using both the chiral NN potential and the pseudo-potential. In Appendix A we present a brief assessment of the deuteron contribution to the second-virial coefficient to show that it is relatively small at the densities and temperatures of interest.

To make a comparison between the HF and virial results for hot matter containing protons we consider neutron-rich matter at temperature $T = 8 \text{ MeV}$ and determine the proton fraction in charge-neutral matter in beta-equilibrium for baryon densities in the range $n_B = 0.0001 - 0.02 \text{ fm}^{-3}$. We solve for the proton and neutron single-particle energies self-consistently and use them to obtain the proton and neutron densities given by

$$n_i = \frac{1}{\pi^2} \int_0^\infty p^2 dp \frac{1}{e^{(p^2/2M_i + \Sigma_i(p) - \mu_i)/T} + 1}. \quad (10)$$

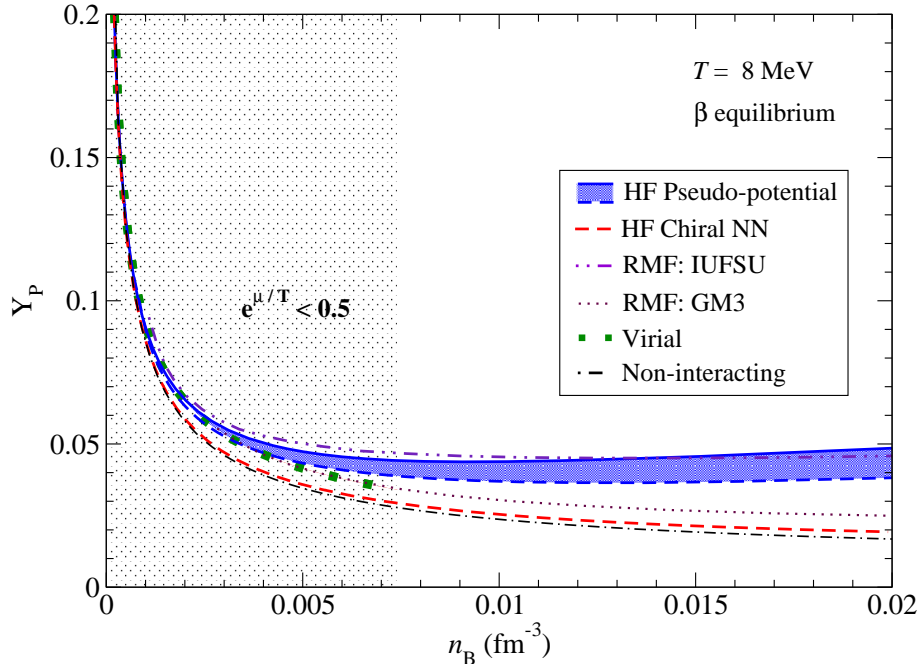


FIG. 4. (Color online) The proton fraction Y_p as a function of density for matter in beta-equilibrium at temperature $T = 8$ MeV. Results for the chiral NN potential and the pseudo-potential in the Hartree-Fock (HF) approximation are shown. The shaded Y_p band is enclosed by solid and dashed lines resulting from the pseudo-potential and modified pseudo-potential calculations, respectively. The region between the HF chiral and HF pseudo-potential band should be considered as a conservative uncertainty range. In addition, we compare to the model-independent virial equation of state [40] as well as the predictions from relativistic mean-field (RMF) theory [23]. The shaded area denotes the density region in which the fugacity $z < 0.5$.

Attractive interactions between neutrons and protons increase the proton fraction Y_p relative to the non-interacting case as is evident from Fig. 4, which shows the proton fraction as a function of the density from different treatments of nuclear interactions. At the lower densities where the virial expansion is reliable, the HF pseudo-potential matches its predictions well. The HF calculation with the chiral potential underestimates the attraction between neutrons and protons and predicts lower values of Y_p .

Since the HF calculation does not provide a reliable treatment of the deuteron pole in the neutron-proton 3S_1 channel, which is nonetheless included in defining the pseudo-potential, we study how the results are affected when we modify the low-energy 3S_1 phase shifts. The alteration is designed to replace the bound state by a scattering resonance at low momentum and to asymptotically match with the experimental values of the phase shifts at high momenta. Further details can be found in Appendix A. By using the original and altered phase shifts in this channel we are able to provide a

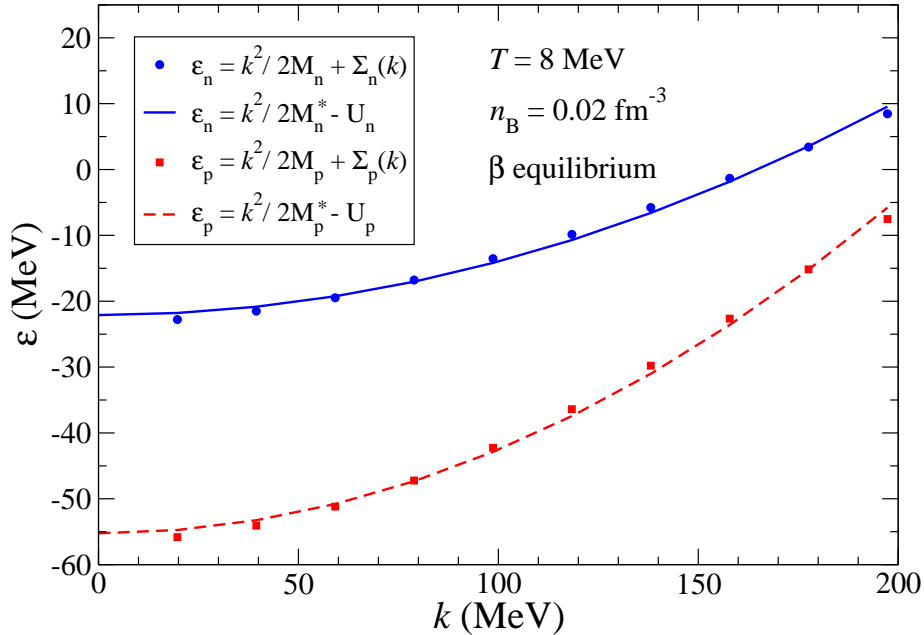


FIG. 5. (Color online) Momentum dependence of the neutron and proton single-particle energies in hot ($T = 8$ MeV) and dense ($n_B = 0.02 \text{ fm}^{-3}$) beta-equilibrated nuclear matter calculated in the HF approximation from the pseudo-potential. The solid and dashed lines are parametrized fits, with the form given in Eq. (11), of the non-relativistic dispersion relations for protons and neutrons respectively.

theoretical band for the prediction of the HF pseudo-potential approach as shown in Fig. 4 and in all future plots where the pseudo-potential results are shown.

The ambient conditions encountered in the neutrino-sphere span densities and temperatures in the range $n_B = 0.001 - 0.05 \text{ fm}^{-3}$ and $T = 3 - 8$ MeV. To study the nuclear medium effects, we choose baryon density $n_B = 0.02 \text{ fm}^{-3}$ and temperature $T = 8$ MeV to compare with earlier results obtained in Ref. [23]. For these conditions the pseudo-potential predicts a proton fraction of $Y_p = 0.049$ (modified pseudo-potential: $Y_p = 0.038$), while for the HF chiral NN potential we find $Y_p = 0.019$. The neutron and proton momentum-dependent single-particle energies associated with mean-field effects from the nuclear pseudo-potential are shown with filled circles and squares in Fig. 5, and qualitatively similar results were found for the chiral NN potential and modified pseudo-potential. For convenience in calculating the charged-current reaction rates described later in the text, we parametrize the momentum dependence

of the single-particle energies with an effective mass plus energy shift:

$$\varepsilon(k) = \frac{k^2}{2M} + \Sigma(k) \simeq \frac{k^2}{2M^*} - U, \quad (11)$$

where U is momentum independent. To demonstrate that the quadratic form in Eq. (11) provides a good description, we display in Fig. 5 the single-particle energies computed for the pseudo-potential (points) and quadratic fit (curves). The results for the proton and neutron effective masses and energy shifts are presented in Table I. The Hartree-Fock energy from the chiral NN potential is considerably smaller for both protons and neutrons than those obtained using the pseudo-potential. The pseudo-potential predictions are also higher than those obtained in the relativistic mean-field (RMF) models employed in recent astrophysical simulations [22, 23]. Simple RMF models such as the GM3 model from Ref. [47] provide a fair description of symmetric nuclei but fail to reproduce ab-initio neutron matter calculations and are therefore not suitable for asymmetric matter calculations. In contrast, a new class of RMF models, such as the IUFSU model from Ref. [48], that are constructed to simultaneously provide a good description of nuclear masses, neutron skin measurements, and match ab-initio calculations of pure neutron matter predict larger energy shifts and are closer in magnitude to those obtained using the HF pseudo-potential approach.

Model	Y_p	M_n^*/M_n	M_p^*/M_p	U_n	U_p	ΔU
HF Pseudo-potential	4.9%	0.65	0.42	22	55	33
HF Pseudo-potential (mod)	3.8%	0.78	0.57	18	42	23
HF Chiral NN	1.9%	0.94	0.90	7	10	3
RMF: GM3	2.5%	0.96	0.96	14	23	9
RMF: IUFSU	4.0%	0.94	0.94	31	52	21
RMF: DD2	4.2%	0.92	0.92	9	25	16

TABLE I. The Hartree-Fock (HF) effective masses M^* and energy shifts U (in units of MeV) for protons and neutrons in beta equilibrium at $n_B = 0.02 \text{ fm}^{-3}$ and temperature $T = 8 \text{ MeV}$. The difference in proton and neutron mean-field shifts is given by $\Delta U = U_p - U_n$, and the proton fraction is denoted by Y_p . Results for both the pseudo-potential and its modified (mod) version are compared to those from the chiral NN interaction and RMF models [23, 49].

In Fig. 6 we show the difference in the neutron and proton self-energies for the chiral NN potential and the pseudo-potential. The momentum dependence is also quite different for these two cases. While the effective masses of proton and neutron quasiparticles are similar and close to bare masses when

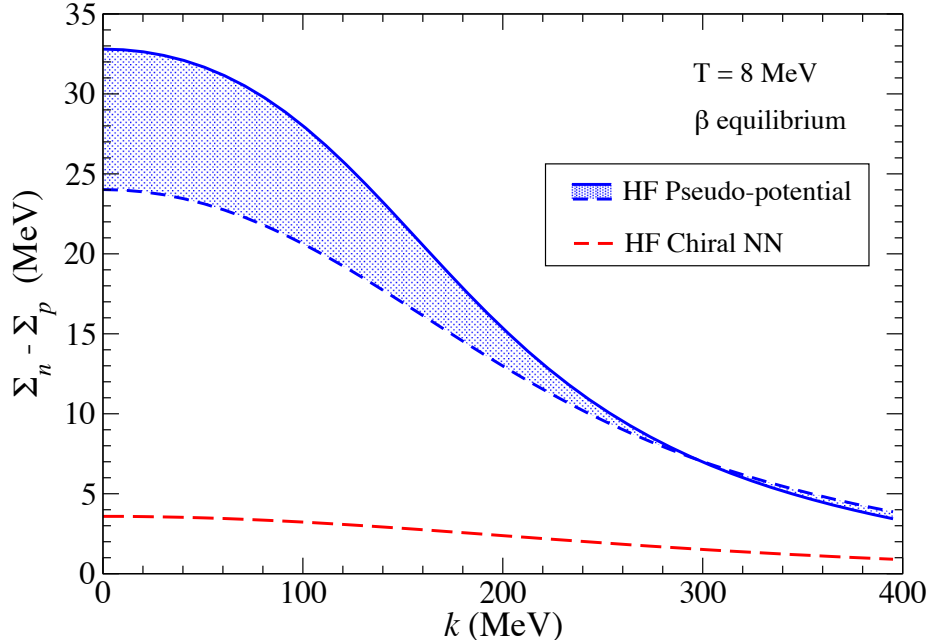


FIG. 6. (Color online) Difference in the momentum-dependent self-energies of neutrons and protons in the HF approximation for beta-equilibrated matter at $n_B = 0.02 \text{ fm}^{-3}$ and temperature $T = 8 \text{ MeV}$. Results for the chiral NN potential and pseudo-potential are shown.

chiral NN interactions are treated in the HF approximation, the implicit iteration of NN interactions in the pseudo-potential results in proton and neutron effective masses that are quite different from each other and much smaller than the free-space masses. The density dependence of self-energy shifts and nucleon effective masses are shown in Figures 7 and 8 respectively. As discussed earlier, the band for the pseudo-potential represents the variation expected for different treatments of the low-momentum behavior of the potential in the deuteron channel. The rapid increase in $\Delta U = U_n - U_p$ and a similarly rapid decrease in the nucleon effective masses obtained in the HF pseudo-potential approach are quite intriguing. Although the HF pseudo-potential approach is well motivated at these low densities and high temperatures as discussed earlier, these predictions for the self-energies are surprisingly large and have to be tested with explicit higher-order calculations in the many-body expansion. For now, it would be reasonable to suppose that the range spanned by the predictions of the HF chiral and HF pseudo-potential approaches represents our current uncertainty associated with non-perturbative effects. Using this as a representative range we discuss in the following section how the energy shifts and effective masses influence the neutrino/antineutrino mean free paths at the temperatures and densities of relevance to the neutrino-sphere.

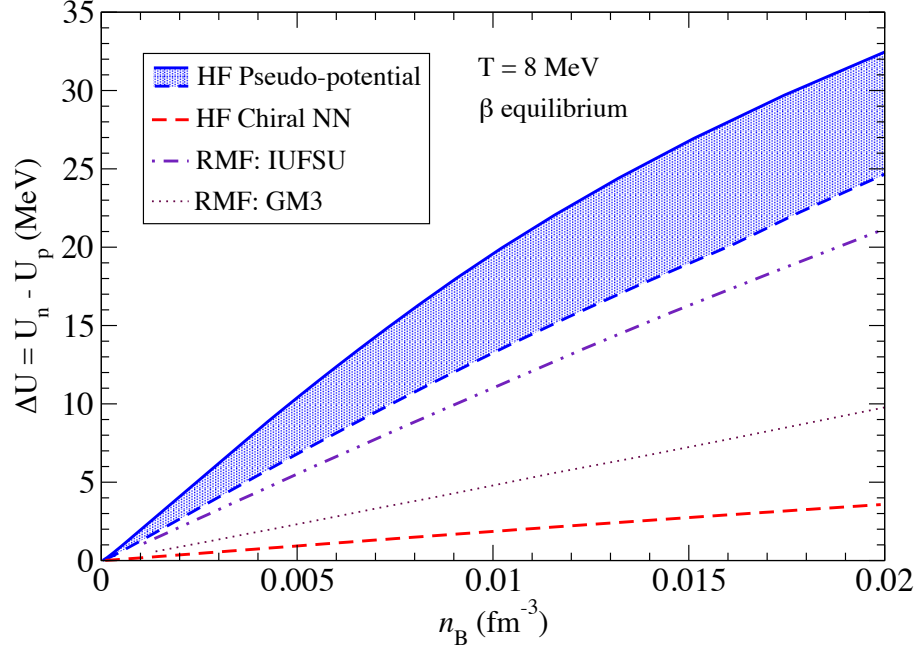


FIG. 7. (Color online) Difference in the HF proton and neutron energy shifts U , defined in Eq. (11), as a function of the density. The results from the pseudo-potential and chiral NN interaction are compared to those from RMF models [23].

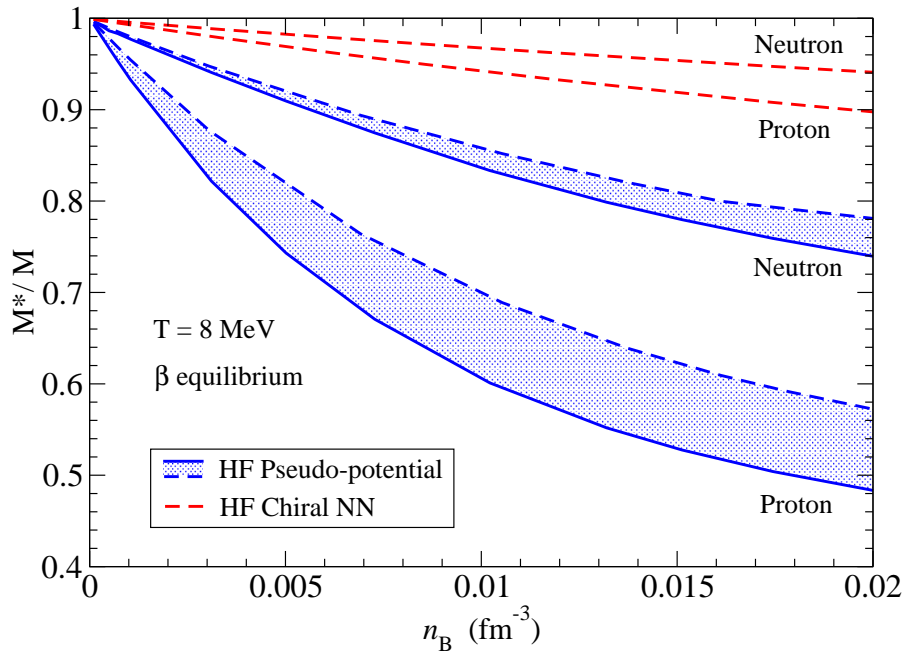


FIG. 8. (Color online) Proton and neutron effective masses M^*/M in the HF approximation as a function of the density for the pseudo-potential and chiral NN interaction.

IV. NEUTRINO ABSORPTION MEAN FREE PATH

The differential cross-section for the reaction $\nu_e + n \rightarrow e^- + p$ follows from Fermi's golden rule and is given by

$$\frac{d\sigma}{V} = \frac{2}{(2\pi)^5} \int d^3p_n d^3p_e d^3p_p \mathcal{W}_{fi} \delta^{(4)}(p_{\nu_e} + p_n - p_e - p_p) f_n(\xi_n)(1 - f_e(\xi_e))(1 - f_p(\xi_p)), \quad (12)$$

where $f(\xi)$ and E are the fermi distribution functions and energies of the particles, and

$$\mathcal{W}_{fi} = \frac{\langle |\mathcal{M}|^2 \rangle}{2^4 E_n E_p E_e E_{\nu_e}} \quad (13)$$

is the transition probability. $\langle |M|^2 \rangle$ is the squared matrix element (corresponding to the diagram in Fig. 9), averaged over initial spin states and summed over the final spin states. For the reaction $\bar{\nu}_e + p \rightarrow e^+ + n$ one obtains a similar expression but with the replacement: $n \leftrightarrow p$, $e^- \rightarrow e^+$, and $\nu_e \rightarrow \bar{\nu}_e$. To simplify notation, we label the incoming neutrino as particle 1 with four-momentum $p_1 = (E_1, \vec{p}_1)$, the incoming baryon as particle 2 with four-momentum $p_2 = (E_2, \vec{p}_2)$, and the outgoing lepton and baryon by the particle labels 3 and 4, with four-momenta $p_3 = (E_3, \vec{p}_3)$ and $p_4 = (E_4, \vec{p}_4)$, respectively.

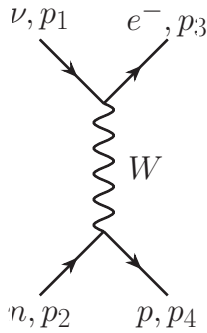


FIG. 9. Tree-level scattering amplitude for the process $\nu_e + n \rightarrow e^- + p$.

In the non-relativistic limit, retaining only terms independent of the nucleon velocity, Eq. (12) simplifies to

$$\frac{1}{V} \frac{d^2\sigma}{d \cos \theta dE_3} = \frac{G_F^2 \cos^2 \theta_C}{4\pi^2} |\vec{p}_3| E_3 (1 - f_3(\xi_3)) \left[(1 + \cos \theta) S_\tau(q_0, q) + g_A^2 (3 - \cos \theta) S_{\sigma\tau}(q_0, q) \right], \quad (14)$$

where $g_A = 1.26$ is the nucleon axial charge, θ is the angle between the initial-state neutrino and the final-state lepton, and θ_C is the Cabibbo angle. $S_\tau(q_0, q)$ and $S_{\sigma\tau}(q_0, q)$ are the response functions associated with the Fermi and Gamow-Teller operators, respectively [23]. The energy transfer to the nuclear medium is $q_0 = E_1 - E_3$, and the magnitude of the momentum transfer to the medium is $q^2 = E_1^2 + E_3^2 - 2E_1E_3 \cos \theta_{13}$, because for the leptons $|\vec{p}_1| = E_1$ and $|\vec{p}_3| = E_3$. In general, the response functions $S_\tau(q_0, q)$ and $S_{\sigma\tau}(q_0, q)$ are different because of isospin and spin-isospin dependent correlations in the medium [3, 4]. However, in the HF approximation $S_\tau(q_0, q) = S_{\sigma\tau}(q_0, q) = S_F(q_0, q)$ where

$$S_F(q_0, q) = \frac{1}{2\pi^2} \int d^3p_2 \delta(q_0 + E_2 - E_4) f(E_2) (1 - f(E_4)), \quad (15)$$

is the response function for a non-interacting Fermi gas, and follows directly from Eq. (12). The effects of interactions are included in Eq. (15) by using the HF self-energies for neutrons and protons calculated in Sec. III. We use the quadratic form defined by Eq. (11):

$$E_2 = M_2 + \frac{p_2^2}{M_2^*} - U_2 \quad \text{and} \quad E_4 = M_4 + \frac{p_4^2}{M_4^*} - U_4, \quad (16)$$

where M_2, M_4 are the physical masses, M_2^*, M_4^* are the effective masses, and U_2, U_4 are the momentum-independent interaction-energy shifts of the initial- and final-state nucleon, respectively. It is also straightforward to include in the nucleon currents corrections due to weak magnetism of order $|\vec{p}|/M$. To do so, we explicitly calculate the square of the matrix element appearing in Eq. (13) for the Fermi weak interaction Lagrangian

$$\mathcal{L} = \frac{G_F}{2\sqrt{2}} \bar{\psi}_4 (g_V \gamma_\mu + i g_M \frac{\sigma_{\mu\nu} q^\nu}{M} - g_A \gamma_\mu \gamma_5) \psi_2 \cdot \bar{e}_3 (\gamma^\mu - \gamma^\mu \gamma^5) \nu_1, \quad (17)$$

where the ψ 's are the nucleon spinors and e and ν are the final-state lepton and initial-state neutrino spinors. The nucleon current has a vector component with $g_V = 1$, an axial-vector component with $g_A = 1.26$, and a Pauli component that incorporates weak magnetism with $g_M = 3.71$ [50]. We find that the differential cross-section per unit volume can be written as

$$\frac{d\sigma(E_1)}{V d\Omega dE_3} = E_3^2 (1 - f_3(E_3)) \int \frac{d^3p_2}{(2\pi)^3} \mathcal{W}_{fi} \delta(E_1 + E_2 - E_3 - E_4) f_2(E_2) (1 - f_4(E_4)). \quad (18)$$

An explicit form for \mathcal{W}_{fi} including weak magnetism and leading $|\vec{p}|/M$ terms in the nucleon weak

currents is derived in Appendix B.

The differential absorption rates for neutrinos and anti-neutrinos are shown in Fig. 10. The rates are shown as a function of the energy of the outgoing lepton (e^- for $\nu_e + n \rightarrow p + e^-$ or e^+ for $\bar{\nu}_e + p \rightarrow n + e^+$) and for an incoming neutrino energy of 24 MeV which is the mean thermal energy $E_\nu \sim 3T = 24$ MeV at the ambient temperature of $T = 8$ MeV. The trends seen in the figure can be understood on the basis of our earlier discussion of reaction kinematics in Sec. II, where it was shown that the interaction-energy shifts in neutron-rich matter enhance the rate for ν_e absorption and suppress the $\bar{\nu}_e$ rate. Further, since the energy shifts are larger and the effective masses are smaller for the pseudo-potential, charged-current rates calculated using the pseudo-potential show larger differences than with the chiral NN potential in the Born approximation.

The inverse neutrino mean free path for the absorption reactions mentioned, $\lambda_\nu^{-1}(E_\nu) = v_{rel}\sigma/V$, where $v_{rel} = c$ is the relative velocity for relativistic neutrinos, can be calculated by numerical integration of the differential cross-section defined in Eq. (18). The results shown in Fig. 11 follow the trends expected from the results for the differential cross-section. The difference between neutrino and anti-neutrino mean free paths is enhanced by the difference between the neutron and proton self-energies, and is larger for the case where the HF self-energy was obtained using the pseudo-potential. Our range for the mean free paths should be compared with those obtained in Refs. [22, 23]. We refer to Fig. 1 in Ref. [22] and Figs. 2 and 3 in Ref. [23] where similar results were obtained using a phenomenological RMF model. Our results are qualitatively similar to those obtained earlier, but important quantitative differences exist. The $\nu_e + n \rightarrow e^- + p$ rate is enhanced by almost a factor of 7 relative to the non-interacting case for $E_\nu = 24$ MeV and the $\bar{\nu}_e + p \rightarrow e^+ + n$ rate is suppressed by a larger factor $\simeq 30$. Under these conditions, neutral current scattering $\bar{\nu}_e + N \rightarrow \bar{\nu}_e + N$ and the inverse bremsstrahlung process $\bar{\nu}_e + \nu_e + N + N \rightarrow N + N$, where N can be either a neutron or a proton, can be expected to be more important. For energy exchange, the latter absorption process will be more relevant and is shown in Fig. 11. Its rate is given by [5]

$$\lambda_{\text{Brems}}^{-1}(\omega_1) = 2\pi G_F^2 n_B \int \frac{d^3\vec{k}_2}{(2\pi)^3} (3 - \cos\theta) f_2 S_A(\omega_1 + \omega_2), \quad (19)$$

where \vec{k}_2 is the momentum of the neutrino, ω_1 and ω_2 are the energies of the anti-neutrino and neutrino, respectively, θ is the scattering angle, and f_2 is the occupation number of the neutrinos. We use the axial

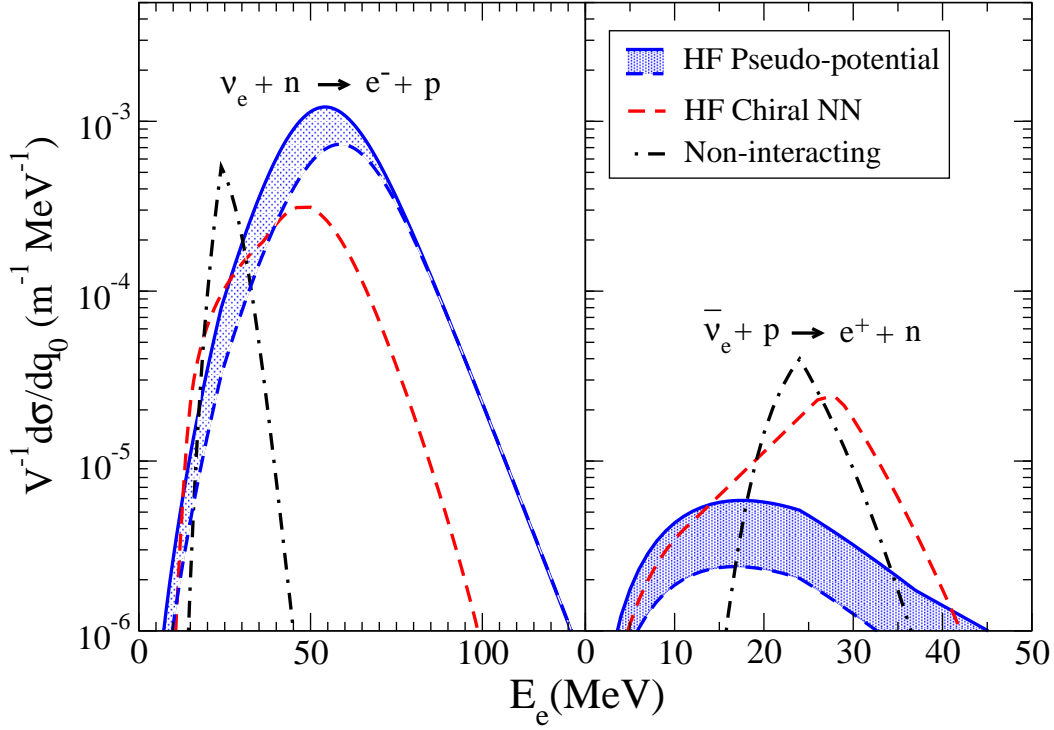


FIG. 10. (Color online) Effect of the in-medium neutron (proton) dispersion relation on the differential cross-section for (anti-)neutrino absorption as a function of the outgoing lepton energy E_e . We consider an incoming neutrino energy $E_\nu = 24$ MeV and matter in beta equilibrium at a density $n_B = 0.02$ fm $^{-3}$ and temperature $T = 8$ MeV, including weak magnetism and leading $|\vec{p}|/M$ corrections. The chiral NN interaction and pseudo-potential are both used in the HF approximation. This provides a range for the theoretical uncertainty due to the many-body treatment, which can be improved by performing higher-order calculations.

response function $S_A(\omega)$ from Ref. [11] and assume a Maxwell-Boltzmann distribution at temperature T for the neutrinos. The inverse mean free path due to the neutrino-pair absorption obtained using the chiral NN potential is shown in red, and results obtained using the full T -matrix potential (corresponding to our pseudo-potential for the self-energy calculations) is shown in blue using consistently the electron fractions and effective masses given in Table I.

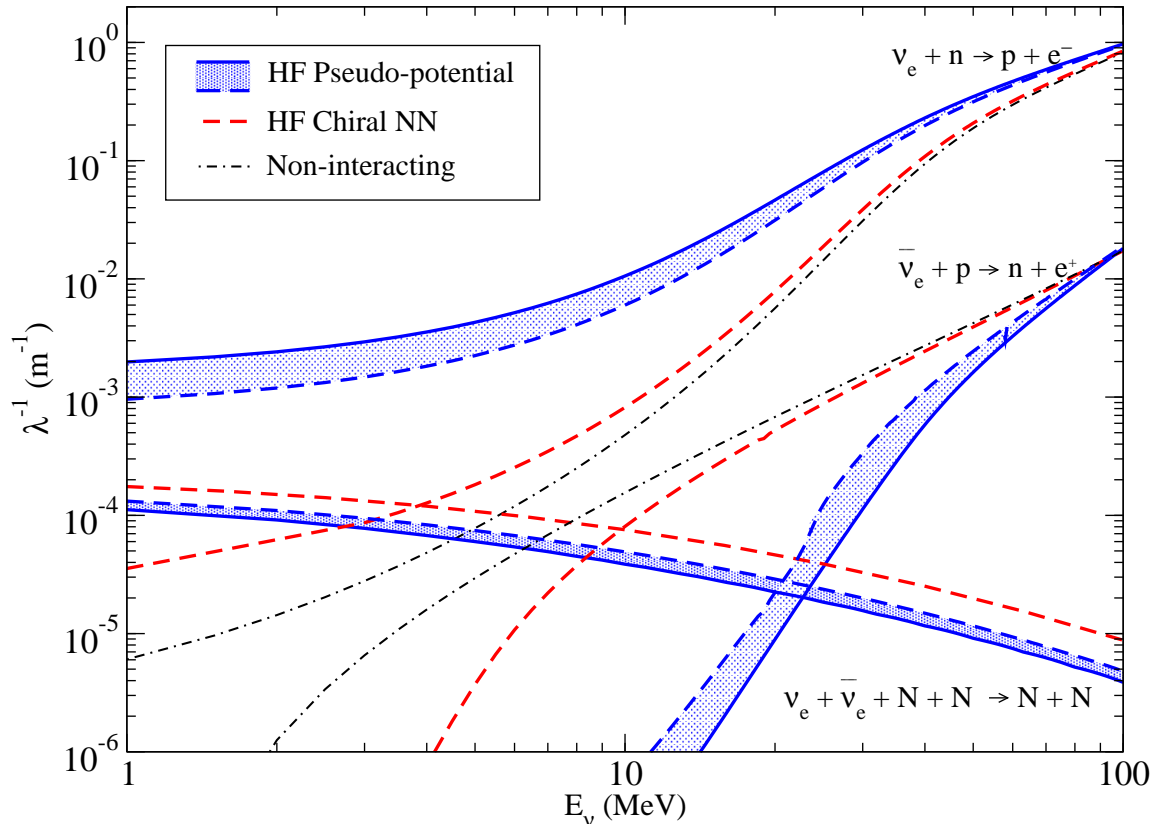


FIG. 11. (Color online) Effect of the in-medium neutron (proton) dispersion relation on the (anti-)neutrino absorption mean free path in beta-equilibrated matter at density $n_B = 0.02 \text{ fm}^{-3}$ and temperature $T = 8 \text{ MeV}$. The chiral NN potential and pseudo-potential are both used in HF approximation. This provides a conservative range for the theoretical uncertainty due to the many-body treatment, which can be improved by performing higher-order calculations. Also shown is the mean free path for the neutrino-pair absorption process.

V. CONCLUSIONS

In this study we have presented a calculation of the HF self-energy of protons and neutrons in the hot neutron-rich matter encountered in the neutrino-sphere of supernovae and used them to calculate the charged-current neutrino and anti-neutrino mean free paths. The mean free paths were found to be quite sensitive to the nucleon dispersion relation, especially to the difference in the energy shifts experienced by neutrons and protons in hot and relatively low-density neutron-rich matter. The difference between the results obtained using a chiral $N^3\text{LO}$ potential and the pseudo-potential is large and indicates that non-perturbative effects in the particle-particle channel, which are approximately included in the pseudo-potential, are important. A desirable feature of the HF pseudo-potential approach is that it reproduces

the predictions of the virial calculation for the energy shifts which are exact in the low-density, high-temperature limit. However, the reader should not assume the results obtained by the pseudo-potential at the densities and temperatures comparable to the ones displayed in Figs. 10 and 11 to be the definitive answer. Instead, it would be prudent to treat the entire region between the HF chiral potential and pseudo-potential as a theoretical band, which needs to be further improved by higher-order many-body calculations. The uncertainty associated with not including the deuteron bound state contribution consistently in the HF pseudo-potential approach was studied by altering the low-momentum 3S_1 phase shift to mimic the behavior expected from a low-energy resonance. This error was found to be relatively small in comparison at the relevant temperatures and densities. Although the RMF model predictions are roughly consistent with the theoretical band it should be noted that they are constrained by fitting to the properties of nuclei, which are largely determined by the behavior at nuclear saturation density and small isospin asymmetry and zero temperature. The error introduced by their extrapolation to low density, large isospin asymmetry and high temperature can be large.

At temperatures lower than those considered in the present work, the importance of Pauli blocking precludes the use of the pseudo-potential, and an alternative strategy would be to employ an in-medium T -matrix as an effective interaction. This framework treats on equal footing quasiparticle energy shifts from the nuclear mean field and Pauli blocking in intermediate states, both of which tend to suppress the role of the strongly attractive components of the nuclear interaction. Consequently, we can expect that the large energy shifts reported in the present study should be reduced in this regime, while at higher temperatures the in-medium T -matrix and pseudo-potential results could be expected to match quantitatively.

The larger difference between neutrino and anti-neutrino rates compared to the predictions of the RMF models will have an impact on supernova nucleosynthesis. To quantitatively gauge its importance it will be necessary to incorporate these new rates into supernova and PNS simulations and predict the resulting neutrino spectra. Qualitatively, we can anticipate a larger $\delta\epsilon$ that would favor smaller Y_e in the neutrino-driven wind compared to the predictions in Ref. [23] based on the RMF models. Simulations that incorporate our current results will be able to ascertain if the change in $\delta\epsilon$ is large enough to favor conditions for a robust r-process in the standard supernova neutrino-driven wind scenario. In addition, our calculations of neutrino cross sections were performed in the impulse approximation. Here we neglect vertex corrections (screening) and finite lifetime effects (damping), which arise because the

weak interaction amplitude involving different nucleons in the system will interfere. These effects were studied within the purview of the RMF model in Ref. [23] and were found not to have as large of an effect as the corrections due to energy shifts because the typical energy and momentum transfer were large compared to characteristic scales associated with temporal and spatial correlations, respectively. Nonetheless, these effects, which are known to be important in the study of neutral-current reactions, warrant further investigation. They can be systematically studied using chiral EFT interactions within self-consistent Green's functions where both particle-particle and particle-hole diagrams in the response function are partially re-summed. At the high densities and temperatures chosen for this study, alpha particles and light clusters are disfavored. However, for a better understanding of a wider range of ambient conditions encountered in the neutrino-sphere, the role of these microphysical effects will need to be investigated and incorporated in proto-neutron star simulations. We plan to explore these topics in future work.

ACKNOWLEDGMENTS

We thank Kai Hebeler, Andreas Lohs, Luke Roberts, and Gang Shen for useful correspondence, and George Bertsch, Charles Horowitz and Gabriel Martínez-Pinedo for useful discussions. The work of E. R. and S. R. was supported in part by grants from NUCLEI SciDAC program and by the DOE Grant No. DE-FG02-00ER41132, J. W. H. acknowledges support from DOE Grant No. DE-FG02-97ER41014, and the work of A. B. and A. S. was supported by a grant from BMBF ARCHES, the ERC Grant No. 307986 STRONGINT, the Helmholtz Alliance HA216/EMMI, and the Studienstiftung des deutschen Volkes. A. S. thanks the Institute for Nuclear Theory at the University of Washington for its hospitality and the DOE for partial support during the completion of this work. This work was also facilitated through the use of advanced computational, storage, and networking infrastructure provided by the Hyak supercomputer system, supported in part by the University of Washington eScience Institute.

[1] S. Reddy, M. Prakash, and J. M. Lattimer, Phys. Rev. D **58**, 013009 (1998).

[2] A. Burrows and R. F. Sawyer, Phys. Rev. C **58**, 554 (1998).

[3] A. Burrows and R. F. Sawyer, Phys. Rev. C **59**, 510 (1999).

- [4] S. Reddy, M. Prakash, J. M. Lattimer, and J. A. Pons, *Phys. Rev. C* **59**, 2888 (1999).
- [5] S. Hannestad and G. Raffelt, *Astrophys. J.* **507**, 339 (1998).
- [6] A. Sedrakian and A. E. L. Dieperink, *Phys. Rev. D* **62**, 083002 (2000).
- [7] C. J. Horowitz and M. A. Pérez-García, *Phys. Rev. C* **68**, 025803 (2003).
- [8] G. I. Lykasov, C. J. Pethick, and A. Schwenk, *Phys. Rev. C* **78**, 045803 (2008).
- [9] S. Bacca, K. Hally, C. J. Pethick, and A. Schwenk, *Phys. Rev. C* **80**, 032802 (2009).
- [10] S. Bacca, K. Hally, M. Liebendörfer, A. Perego, C. J. Pethick, and A. Schwenk, *Astrophys. J.* **758**, 34 (2012).
- [11] A. Bartl, C. Pethick, and A. Schwenk, *Phys. Rev. Lett.* **113**, 081101 (2014).
- [12] J. A. Pons, S. Reddy, M. Prakash, J. M. Lattimer, and J. A. Miralles, *Astrophys. J.* **513**, 780 (1999).
- [13] L. Hüdepohl, B. Müller, H.-T. Janka, A. Marek, and G. G. Raffelt, *Phys. Rev. Lett.* **104**, 251101 (2010).
- [14] L. F. Roberts, G. Shen, V. Cirigliano, J. A. Pons, S. Reddy, and S. E. Woosley, *Phys. Rev. Lett.* **108**, 061103 (2012).
- [15] H.-T. Janka, *Ann. Rev. Nucl. Part. Sci.* **62**, 407 (2012).
- [16] Y.-Z. Qian and S. E. Woosley, *Astrophys. J.* **471**, 331 (1996).
- [17] A. Arcones and F.-K. Thielemann, *J. Phys. G* **40**, 013201 (2013).
- [18] K. Scholberg, *Ann. Rev. Nucl. Part. Sci.* **62**, 81 (2012).
- [19] R. D. Hoffman, S. E. Woosley, and Y.-Z. Qian, *Astrophys. J.* **482**, 951 (1997).
- [20] S. Wanajo, *Astrophys. J.* **770**, L22 (2013).
- [21] T. Fischer, G. Martínez-Pinedo, M. Hempel, and M. Liebendörfer, *Phys. Rev. D* **85**, 083003 (2012).
- [22] G. Martínez-Pinedo, T. Fischer, A. Lohs, and L. Huther, *Phys. Rev. Lett.* **109**, 251104 (2012).
- [23] L. F. Roberts, S. Reddy, and G. Shen, *Phys. Rev. C* **86**, 065803 (2012).
- [24] C. J. Horowitz, G. Shen, E. O'Connor, and C. D. Ott, *Phys. Rev. C* **86**, 065806 (2012).
- [25] D. R. Entem and R. Machleidt, *Phys. Rev. C* **68**, 041001 (2003).
- [26] L. Tolos, B. Friman, and A. Schwenk, *Nucl. Phys. A* **806**, 105 (2008).
- [27] K. Hebeler and A. Schwenk, *Phys. Rev. C* **82**, 014314 (2010).
- [28] K. Hebeler, S. K. Bogner, R. J. Furnstahl, A. Nogga, and A. Schwenk, *Phys. Rev. C* **83**, 031301 (2011).
- [29] I. Tews, T. Krüger, K. Hebeler, and A. Schwenk, *Phys. Rev. Lett.* **110**, 032504 (2013).
- [30] A. Gezerlis, I. Tews, E. Epelbaum, S. Gandolfi, K. Hebeler, A. Nogga, and A. Schwenk, *Phys. Rev. Lett.*

111, 032501 (2013).

- [31] L. Coraggio, J. W. Holt, N. Itaco, R. Machleidt, and F. Sammarruca, *Phys. Rev. C* **87**, 014322 (2013).
- [32] J. W. Holt, N. Kaiser, G. A. Miller, and W. Weise, *Phys. Rev. C* **88**, 024614 (2013).
- [33] T. Krüger, I. Tews, K. Hebeler, and A. Schwenk, *Phys. Rev. C* **88**, 025802 (2013).
- [34] G. Hagen, T. Papenbrock, A. Ekstrom, K. Wendt, G. Baarden, S. Gandolfi, M. Hjorth-Jensen, and C. J. Horowitz, *Phys. Rev. C* **89**, 014319 (2014).
- [35] C. Drischler, V. Somà, and A. Schwenk, *Phys. Rev. C* **89**, 025806 (2014).
- [36] L. Coraggio, J. W. Holt, N. Itaco, R. Machleidt, L. E. Marcucci, and F. Sammarruca, *Phys. Rev. C* **89**, 044321 (2014).
- [37] C. Wellenhofer, J. W. Holt, N. Kaiser, and W. Weise, *Phys. Rev. C* **89**, 064009 (2014).
- [38] V. G. J. Stoks, R. A. M. Klomp, M. C. M. Rentmeester, and J. J. de Swart, *Phys. Rev. C* **48**, 792 (1993), <http://nn-online.org>.
- [39] C. J. Horowitz and A. Schwenk, *Nucl. Phys. A* **776**, 55 (2006).
- [40] C. J. Horowitz and A. Schwenk, *Phys. Lett. B* **638**, 153 (2006).
- [41] G. D. Mahan, *Many-Particle Physics*, 2nd ed. (Plenum, New York, N.Y., 1993).
- [42] N. Fukuda and R. G. Newton, *Phys. Rev.* **103**, 1558 (1956).
- [43] W. B. Riesenfeld and K. M. Watson, *Phys. Rev.* **104**, 492 (1956).
- [44] G. Röpke, *Phys. Rev. C* **79**, 014002 (2009).
- [45] S. Typel, G. Röpke, T. Klähn, D. Blaschke, and H. H. Wolter, *Phys. Rev. C* **81**, 015803 (2010).
- [46] M. Hempel, J. Schaffner-Bielich, S. Typel, and G. Röpke, *Phys. Rev. C* **84**, 055804 (2011).
- [47] N. K. Glendenning and S. A. Moszkowski, *Phys. Rev. Lett.* **67**, 2414 (1991).
- [48] F. J. Fattoyev, C. J. Horowitz, J. Piekarewicz, and G. Shen, *Phys. Rev. C* **82**, 055803 (2010).
- [49] G. Martínez-Pinedo, T. Fischer, and L. Huther, *J. Phys. G.* **41**, 044008 (2014).
- [50] C. J. Horowitz, *Phys. Rev. D* **65**, 043001 (2002).
- [51] C. J. Horowitz and G. Li, *Phys. Rev. D* **61**, 063002 (2000).

Appendix A: Deuteron contribution and the modified pseudo-potential

To assess the importance of the deuteron pole in neutron-proton scattering we study its contribution in the second-order virial calculation. Since the contributions to the second virial coefficient from the bound state denoted by b^d and the scattering continuum denoted by b^s can be calculated separately [39], the ratio

$$r = \frac{b^s}{b^s + b^d}, \quad (\text{A1})$$

is a measure of the relative importance of the scattering continuum. In the virial calculation r is independent of density and increases rapidly with temperature as shown in Fig. 12. At the physical value of the deuteron binding energy the contribution from the scattering continuum is about 70% at $T = 8$ MeV. Medium effects mentioned earlier reduce the deuteron binding energy, and although such changes to B_d are beyond the scope of the virial expansion, it is still useful to explore how the ratio r changes for smaller values of B_d .

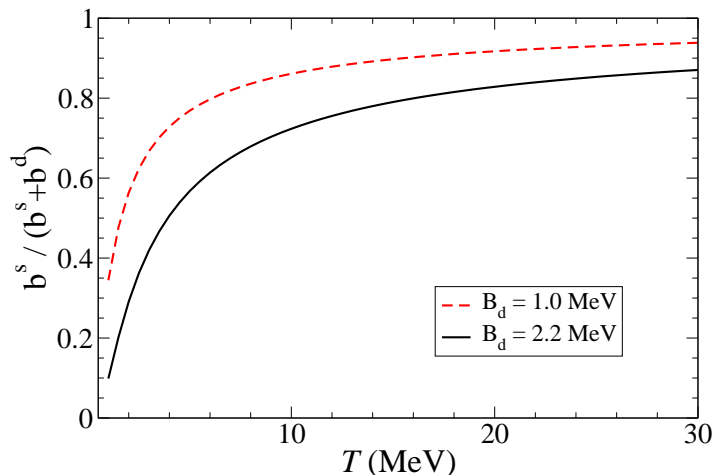


FIG. 12. (Color online) The relative importance of the scattering continuum contribution to the second virial coefficient (normalized with respect to the sum of bound- and scattering-state contributions). Results assuming a free-space deuteron binding energy and a medium-reduced binding energy of $B_d = 1.0$ MeV are shown.

The red-dashed curve in Fig. 12 was obtained by setting $B_d = 1$ MeV and shows how dramatically the deuteron contribution decreases with B_d . Model calculations of the reduction in the deuteron binding energy predict $B_d < 1$ MeV for $n_B > 0.005$ fm $^{-3}$ for typical temperatures in the range $T =$

5 – 10 MeV [45].

The neutron-proton scattering phase shift at low energies in the 3S_1 channel is dominated by the deuteron bound state and by Levinson’s theorem is set equal to π at zero momentum. This complicates the definition of the pseudo-potential that is to be used in the Born approximation since the potential constructed does not explicitly include these negative energy states. This in principle restricts the use of the pseudo-potential to large temperatures where we expect the deuteron abundances to be small. To assess the importance of the low-momentum behavior of the 3S_1 phase shifts we have modified them by hand. The modified potential mimics the low-momentum behavior expected for a resonance close to zero energy and asymptotically matches the original values of the 3S_1 phase shift at high momenta. We show both the original and modified versions of the 3S_1 phase shifts in Fig. 13.

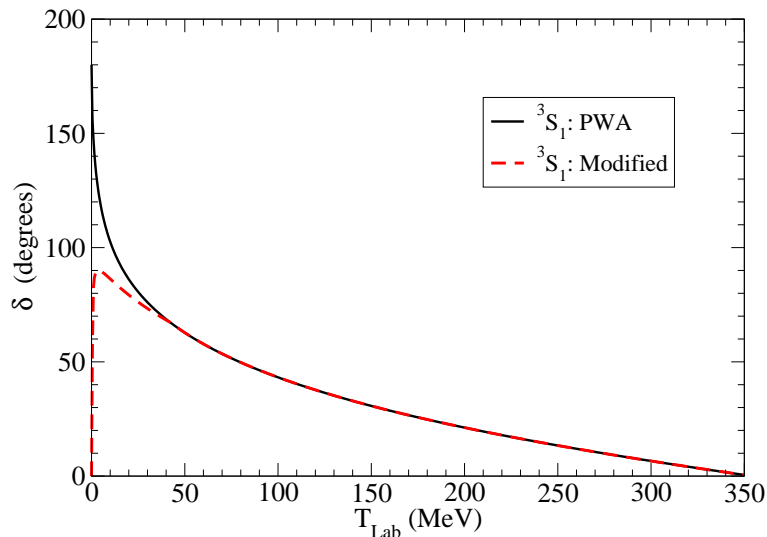


FIG. 13. (Color online) 3S_1 phase shift as a function of laboratory energy T_{lab} from the Nijmegen partial-wave analysis (PWA) [38] as well as those used in the modified pseudo-potential.

Appendix B: Transition rate including weak magnetism for non-relativistic nucleons

Here we derive expressions for the transition rate \mathcal{W}_{fi} including the contribution from weak magnetism. We shall consider thermal neutrinos with energy $E_\nu \simeq T$ and calculate \mathcal{W}_{fi} to linear order in T/M where M is the average nucleon mass. The expressions are derived for neutrinos, and

analogous expression for anti-neutrinos are obtained by the substitution $\{g_V, g_M\} \rightarrow \{-g_V, -g_M\}$.

The transition rate

$$\mathcal{W}_{fi} = \frac{\langle |\mathcal{M}|^2 \rangle}{2^4 E_1 E_2 E_3 E_4}, \quad (\text{B1})$$

where

$$\begin{aligned} \langle |\mathcal{M}|^2 \rangle &= \frac{1}{8} G_F^2 \text{Tr} \left[\gamma^\mu (1 - \gamma^5) \not{p}_1 \gamma^\nu (1 - \gamma^5) \not{p}_3 \right] \\ &\times \text{Tr} \left\{ \left[\gamma_\mu (g_V - g_A \gamma^5) + i g_M \frac{\sigma_{\mu\alpha} q^\alpha}{M} \right] (\not{p}_2 + M_2) \left[\gamma_\nu (g_V - g_A \gamma^5) - i g_M \frac{\sigma_{\nu\alpha} q^\alpha}{M} \right] (\not{p}_4 + M_4) \right\} \\ &\equiv 8 G_F^2 (\langle |\mathcal{M}|^2 \rangle^{VA} + \langle |\mathcal{M}|^2 \rangle^{VAM} + \langle |\mathcal{M}|^2 \rangle^M). \end{aligned} \quad (\text{B2})$$

is the square of the matrix element summed over final-state spins and averaged over initial-state spins for the interaction in Eq. (17). Here, the vector-axial part is given by

$$\langle |\mathcal{M}|^2 \rangle^{VA} = (g_A - g_V)^2 (p_1 \cdot p_4)(p_2 \cdot p_3) + (g_A + g_V)^2 (p_1 \cdot p_2)(p_3 \cdot p_4) + (g_A^2 - g_V^2) M_2 M_4 (p_1 \cdot p_3), \quad (\text{B3})$$

the mixed term is given by

$$\begin{aligned} \langle |\mathcal{M}|^2 \rangle^{VAM} &= -\frac{g_M}{M} \left\{ (p_1 \cdot q) \left[(2g_A - g_V) M_4 (p_2 \cdot p_3) + (2g_A + g_V) M_2 (p_3 \cdot p_4) \right] + (p_4 \cdot q) g_V M_2 (p_1 \cdot p_3) \right. \\ &\quad \left. - (p_2 \cdot q) g_V M_4 (p_1 \cdot p_3) - (p_3 \cdot q) \left[2(g_A + g_V) M_4 (p_1 \cdot p_2) - (2g_A - g_V) M_2 (p_1 \cdot p_4) \right] \right\}, \end{aligned} \quad (\text{B4})$$

and the contribution due to weak magnetism is given by

$$\begin{aligned} \langle |\mathcal{M}|^2 \rangle^M &= \frac{g_M^2}{M^2} \left\{ (p_1 \cdot q) \left[(p_2 \cdot q)(p_3 \cdot p_4) - (M_2 M_4 + p_2 \cdot p_4)(p_3 \cdot q) + (p_2 \cdot p_3)(p_4 \cdot q) \right] \right. \\ &\quad \left. + (p_3 \cdot q) \left[(p_1 \cdot p_4)(p_2 \cdot q) + (p_1 \cdot p_2)(p_4 \cdot q) \right] \right. \\ &\quad \left. - q^2 \left[(p_1 \cdot p_3)(M_2 M_4 - p_2 \cdot p_4) + 2[(p_1 \cdot p_4)(p_2 \cdot p_3) + (p_1 \cdot p_2)(p_3 \cdot p_4)] \right] \right\}. \end{aligned} \quad (\text{B5})$$

Setting $q^\mu = p_1^\mu - p_3^\mu$, we find that these results confirm equations (11) and (12) in Ref. [51].

At this stage we have only neglected the electron and neutrino masses because they are small compared

to the thermal energies of the lepton $E_1 \simeq |\vec{p}_1| \sim T$ and $E_3 \simeq |\vec{p}_3| \sim T$. In addition, for typical ambient conditions we consider here, nucleons are non-relativistic and non-degenerate thus $|\vec{p}_2| \sim \sqrt{MT}$ and $|\vec{p}_4| \sim \sqrt{MT}$. Since the nucleon mass is large compared to the temperature it is useful to define the following expansion parameters

$$\begin{pmatrix} \{\chi_1, \chi_3, \chi_0\} \\ \{v_2, v_4, \chi_q\} \end{pmatrix} \equiv \begin{pmatrix} \{E_1/M, E_3/M, q_0/M\} \\ \{|\vec{p}_2|/M, |\vec{p}_4|/M, |\vec{q}|/M\} \end{pmatrix} \sim \begin{pmatrix} T/M \\ \sqrt{T/M} \end{pmatrix} \quad (\text{B6})$$

where elements in the first row are parametrical of order T/M and elements in the second row are order $\sqrt{T/M}$. Using energy-momentum conservation, $p_4^\mu = p_1^\mu + p_2^\mu - p_3^\mu$ and expanding to linear order in T/M we find that

$$\begin{aligned} \mathcal{W}_{fi} &\approx \frac{G_F^2}{2} \times \left\{ \left[g_V^2(1 + \eta_{13}) + g_A^2(3 - \eta_{13}) \right] \right. && \mathcal{O}(1) \\ &+ \left[2 g_M g_A \chi_q (\eta_{1q} - \eta_{3q}) - (g_A^2 + g_V^2) v_2 (\eta_{12} + \eta_{23}) \right] && \mathcal{O}\left(\sqrt{\frac{T}{M}}\right) \\ &+ \left[\frac{1}{2} \left[(g_A + g_V)^2 \chi_1 - (g_A - g_V)^2 \chi_3 \right] (1 - \eta_{13}) + (g_A^2 + g_V^2) v_2^2 \eta_{12} \eta_{23} \right. \\ &\quad \left. + 2 g_M g_A v_2 \chi_q (\eta_{12} \eta_{3q} - \eta_{1q} \eta_{23}) + g_M^2 \chi_q^2 (1 - \eta_{1q} \eta_{3q}) \right] \left. \right\} && \mathcal{O}\left(\frac{T}{M}\right) \end{aligned}$$

where the first line contains terms of $\mathcal{O}(1)$, the second line contain terms of $\mathcal{O}(\sqrt{T/M})$ and the third and fourth lines contains terms of $\mathcal{O}(T/M)$. The angles between three vectors \vec{p}_i and \vec{p}_j is denoted by η_{ij} and the angle between \vec{p}_i and \vec{q} is denoted by η_{iq} .